

Probing super-heavy dark matter with ultra-high-energy gamma rays

Marco Chianese,^{1, 2, *} Ninetta Saviano,^{2, 1, †} Sara Cesare,^{1, 2} Vincenzo M. Grieco,^{1, 2} Valentina Nasti,^{1, 2} Francesca Spinnato,^{1, 2} and Alessandro Tiano^{1, 2}

¹*Scuola Superiore Meridionale, Via Mezzocannone 4, 80138 Napoli, Italy*

²*INFN - Sezione di Napoli, Complesso Universitario Monte Sant'Angelo, 80126 Napoli, Italy*

We refine the constraints on the lifetime of decaying super-heavy dark matter particles (SHDM), with masses ranging from 10^7 to 10^{15} GeV, by analyzing ultra-high-energy (UHE) gamma-ray data. Our approach involves an accurate comparison of the primary gamma-ray emissions resulting from prompt SHDM decays in the galactic halo with the most recent upper limits on isotropic UHE gamma-ray fluxes provided by various extensive air shower experiments. We demonstrate that a precise consideration of the field of view and the geometric acceptance of different UHE gamma-ray observatories has significant implications for the inferred limits of dark matter lifetime. In addition, we examine the influence of uncertainties linked to the current models of the galactic dark matter distribution, employing diverse halo density profiles while varying both their radial extent and the local dark matter density. Our findings indicate that the newly established UHE gamma-ray constraints are marginally less stringent than earlier evaluations, thereby revisiting the SHDM parameter space and allowing for observable neutrino fluxes.

CONTENTS

I. Introduction	1
II. Geometrical acceptance efficiency of the experiments	2
III. Gamma-ray flux from heavy decaying dark matter	6
A. Gamma-ray attenuation in the Milky Way	6
B. Dark matter distribution and \mathcal{D} -factor	8
IV. Constraints on the dark matter lifetime	9
V. Conclusions	12
Acknowledgements	12
References	13
A. Lifetime bounds for several decay channels	17

I. INTRODUCTION

Within the Λ CDM paradigm, approximately 26% of the Universe's matter-energy budget consists of a nonrelativistic, pressureless component, referred to as dark matter (DM), which interacts almost exclusively through gravity. [1–5]. Among the various strategies to probe DM particles, indirect detection searches play a central role by seeking the Standard Model (SM) byproducts of DM annihilation or decay in astrophysical environments. Motivated by the absence of clear signals from DM particles in the GeV–TeV mass range, increasing attention has shifted toward scenarios with super-heavy dark matter (SHDM) that can decay on cosmological timescales [6–17]. In such models, the dark matter lifetime is much longer than the age of the Universe, ensuring consistency with cosmological and astrophysical observations, while rare decay events can still produce observable fluxes of SM particles, notably cosmic rays, high-energy neutrinos, and Ultra-High-Energy (UHE) gamma rays [18–51]. Interestingly, decaying SHDM particles have been proposed as a possible explanation of the recent KM3NeT/ARCA observation of a neutrino event with

* m.chianese@ssmeridionale.it

† nsaviano@na.infn.it

an energy of approximately 220 PeV [52–59]. Hence, it is crucial to assess the viability of this scenario by robustly quantifying the allowed SHDM parameter space from a multi-messenger perspective.

In this work, we examine the prompt gamma-ray emission of decaying SHDM particles with masses from 10^7 to 10^{15} GeV, originating from the galactic DM halo, for several decay channels. Hence, we derive the constraints on the SHDM lifetime by exploiting the latest upper bounds on the isotropic flux of UHE gamma rays placed by the extensive air shower (EAS) experiments CASA-MIA [60], KASCADE [61], KASCADE-Grande [62], Telescope Array (TA) [63] and Pierre Auger Observatory (PAO) [64–67]. Not only do these observatories probe the UHE gamma-ray sky over complementary energy ranges, but also have distinct sky coverages and sensitivities, owing to their different latitudes and zenith-angle acceptances. We improve upon previous SHDM analyses by explicitly accounting for the field of view (FOV) and the geometrical acceptance efficiency of each experiment. As a result, the \mathcal{D} -factor, which represents the line-of-sight integral of the DM density, varies between experiments, thus influencing the DM constraints. Moreover, we adopt updated parameter values for two representative galactic DM halo models, namely the generalized Navarro-Frenk-White (gNFW) and the Burkert density profiles, and assess the robustness of the resulting SHDM lifetime constraints with respect to the uncertainties on determination of the galactic DM distribution [68, 69].

The paper is organized as follows. In section II, we define and compute the geometrical acceptance efficiency for the EAS experiments considered in this study. In Section III, we present a detailed calculation of the UHE gamma-ray flux produced by decaying SHDM particles, with particular emphasis on the galactic gamma-ray attenuation and on the evaluation of the energy-dependent \mathcal{D} -factor for both the DM density profiles. In Section IV, we outline the statistical methodology and report the resulting lower bounds on the SHDM lifetime derived from the latest UHE gamma-ray data. Finally, in Section V, we draw the main conclusions of this work.

II. GEOMETRICAL ACCEPTANCE EFFICIENCY OF THE EXPERIMENTS

The response of a ground-based observatory is inherently non-uniform, as only the directions encompassed within its FOV contribute to the events detected at any given time. The UHE gamma-ray observatories analyzed in this work (see Tab. I for a concise summary of their primary parameters) possess significantly varying sky coverage and sensitivity, owing to their unique geographical latitudes and zenith-angle acceptances. It is therefore imperative to account for this directional dependency when investigating anisotropic gamma-ray fluxes, such as those expected from DM decays. As will be discussed in the subsequent section, the DM-induced gamma-ray flux is influenced by the spatial distribution of the galactic halo, and is thus intrinsically anisotropic. In order to describe the geometrical efficiency of a detector, we utilize and expand upon the framework presented in Ref. [70]. The initial consideration within this framework is the definition of the instantaneous aperture A_{eff} , which serves to quantify the effective collecting area for particles originating from a specified direction in the sky. This aperture is contingent upon several factors, including the zenith angle θ_z , the azimuth φ and in general on the energy E_γ of the incoming events [71]. Specifically, we have

$$A_{\text{eff}}(\theta_z(t), \varphi(t), E_\gamma) = A(E_\gamma) \cdot \cos \theta_z(t) \cdot \epsilon(\theta_z(t), \varphi(t), E_\gamma), \quad (1)$$

where $A(E_\gamma)$ represents the physical geometric area of the detector, $\cos \theta_z(t)$ serves as the geometric factor that accounts for the projection of the detection area relative to the direction of incoming particles and ϵ denotes the detection efficiency. For a detector located at latitude λ , we adopt the standard assumptions employed in wide-field, ground-based EAS experiments [70, 72]:

1. *Full-time operation*: the detector acquires data over a full sidereal day;
2. *Azimuthal symmetry*: the aperture is uniform with respect to azimuth (or right ascension in equatorial coordinates);
3. *Separable geometric term*: although the instantaneous aperture in Eq. (1) generally depends on both the arrival direction and the event energy, we adopt a simplified treatment in which the geometrical contribution is factorized from the detector energy response. For each fixed energy E_γ we therefore treat $A(E_\gamma)$ as an effective constant geometrical area A_0 (i.e. we evaluate the angular exposure per energy bin), allowing us to isolate the angular dependence of the exposure.
4. *Full efficiency* within a zenith cut θ_m characteristic of the experiment:

$$\epsilon(\theta_z(t)) = \begin{cases} 1, & \theta_z(t) \leq \theta_m, \\ 0, & \theta_z(t) > \theta_m. \end{cases} \quad (2)$$

Experiment	Latitude (°)	Zenith angle range (°)	Energy range (GeV)
CASA-MIA [60]	40.2	0 – 60	$3.26 \times 10^5 – 3.33 \times 10^7$
KASCADE [61]	49.1	0 – 18	$2.45 \times 10^5 – 1.84 \times 10^7$
KASCADE-Grande [62]	49.1	0 – 40	$1.50 \times 10^6 – 2.92 \times 10^8$
TA [63]	39.3	0 – 55	$1.00 \times 10^9 – 9.92 \times 10^{10}$
PAO UMD + SD 433 m [64]	–35.2	0 – 52	$5.00 \times 10^7 – 2.00 \times 10^8$
PAO HECO + SD 750 m [65]	–35.2	0 – 60	$2.00 \times 10^8 – 1.00 \times 10^9$
PAO Hybrid [66]	–35.2	0 – 60	$1.00 \times 10^9 – 9.96 \times 10^9$
PAO SD 1500 m [67]	–35.2	30 – 60	$9.96 \times 10^9 – 3.98 \times 10^{10}$

TABLE I. Summary of the key parameters of the EAS experiments considered in this work, including latitude, zenith angle acceptance and energy range.

Under these considerations, the sole factor governing the instantaneous aperture is the geometric projection $\cos \theta_z(t)$. Consequently, the equation for the effective collecting area Eq. (1) reduces to

$$A_{\text{eff}}(\theta_z(t)) = A_0 \cos \theta_z(t) _{\theta_z(t) \leq \theta_m}, \quad (3)$$

where the condition $\theta_z(t) < \theta_m$ encodes the visibility of the source within the FOV of the detector. From the instantaneous aperture, we can compute the exposure $\mathcal{E}(\alpha, \delta)$ for a source at right ascension α and declination δ as [70]

$$\mathcal{E}(\alpha, \delta) = \int A_{\text{eff}}(t) dt. \quad (4)$$

This function quantifies both the duration and efficacy of the detector's observation of a specific direction, incorporating the Earth's rotational dynamics. In the case of a continuously operating, azimuthally symmetric array, all sources situated along the same declination circle are observed identically throughout a sidereal day. This indicates that the exposure is invariant with respect to the parameter α , and it suffices to evaluate only $\mathcal{E}(\delta)$. By substituting time with the local hour angle H , under the transformation $dH = \omega_{\text{Earth}} dt$, and limiting the integral to those intervals when the source remains within the zenith cut ($\theta_z \leq \theta_m$), we obtain:

$$\mathcal{E}(\delta) = \frac{A_0}{\omega_{\text{Earth}}} \int_{H \in \text{visible}} \cos \theta_z(\lambda, \delta; H) dH, \quad (5)$$

where ω_{Earth} is the Earth's sidereal angular velocity. From spherical trigonometry, the projection factor $\cos \theta_z$ can be expressed as a function of the hour angle as [73]

$$\sin h(\lambda, \delta; H) = \cos \theta_z(\lambda, \delta; H) = \sin \lambda \sin \delta + \cos \lambda \cos \delta \cos H. \quad (6)$$

A source is visible as long as its altitude $h = 90^\circ - \theta_z$ exceeds the minimum altitude $h_m = 90^\circ - \theta_m$, leading to the following condition

$$\cos H \geq \frac{\cos \theta_m - \sin \lambda \sin \delta}{\cos \lambda \cos \delta}. \quad (7)$$

We define α_m as the maximum hour angle at which the celestial source remains within the field of view of the experiment positioned at latitude λ on Earth:

$$\alpha_m = \cos^{-1} \left[\frac{\cos \theta_m - \sin \lambda \sin \delta}{\cos \lambda \cos \delta} \right] = \cos^{-1} \xi. \quad (8)$$

Consequently, the observable range of hour angles is given by $H \in [-\alpha_m, +\alpha_m]$. Therefore, α_m quantifies the half-arc of visibility with the limits [70]:

$$\begin{cases} \alpha_m = 0 & \text{if } \xi > 1 \quad (\text{the source is never observable}) \\ \alpha_m = \pi & \text{if } \xi < -1 \quad (\text{the source is circumpolar, i.e. always observable}) \\ \alpha_m = \cos^{-1} \xi & \text{if } -1 < \xi < 1. \end{cases}$$

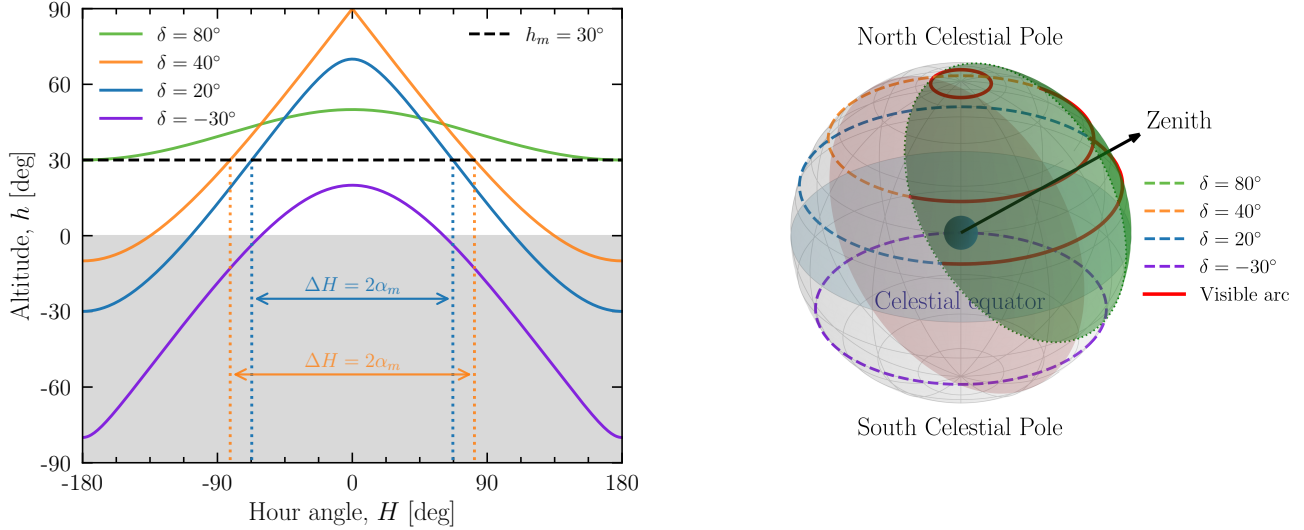


FIG. 1. Geometrical interpretation of the visibility condition for a detector located at latitude $\lambda = 40^\circ$ and with a zenith cut $\theta_m = 60^\circ$. The left plot shows the altitude curves and the corresponding visible hour-angle intervals for selected declinations. The visibility interval $\Delta H = 2\alpha_m$ corresponds to the portion of trajectory lying above the minimum altitude h_m . The graphic on the right shows the same trajectories projected on the celestial sphere together with the detector FOV (green shaded area). The red arc denotes the portion of each trajectory lying above the minimum altitude and thus contributing to the exposure.

Moreover, from Eq. (6) we observe that, when the source passes the local meridian corresponding to $H = 0$, it reaches the maximum altitude h_{\max} equal to

$$h_{\max} = \sin^{-1}(\cos(\delta - \lambda)) . \quad (9)$$

Imposing the visibility condition $h_{\max} \geq 90^\circ - \theta_m$, the range of declination circles that fall within the FOV of an experiment is

$$\lambda - \theta_m \leq \delta \leq \lambda + \theta_m . \quad (10)$$

In particular, declinations satisfying $\delta = \lambda$ correspond to trajectories that reach the maximum elevation accessible from the detector site. Such transits occur at the smallest zenith angles and therefore benefit from the most favorable observing conditions. The geometrical role of α_m , the detector FOV and the geometric considerations discussed above are illustrated in Fig. 1. The plot on the left shows how different declinations produce different altitude tracks and visibility intervals, while the graphic on the right illustrates the corresponding geometric interpretation on the celestial sphere.

Substituting Eq. (6) into Eq. (5) and integrating over the visible range yields

$$\mathcal{E}(\delta) = \frac{A_0}{\omega_{\text{Earth}}} \int_{-\alpha_m}^{+\alpha_m} \cos \theta_z(\lambda, \delta; H) dH = \frac{2A_0}{\omega_{\text{Earth}}} (\alpha_m \sin \lambda \sin \delta + \cos \lambda \cos \delta \sin \alpha_m) . \quad (11)$$

We can now introduce the geometrical acceptance efficiency $\omega(\delta)$ as the function that quantifies the relative exposure of a ground-based detector at latitude λ to a circle of declination δ [70]. We define it by normalizing the exposure to its maximum possible value on the celestial sphere, corresponding to an ideal circumpolar source that remains constantly at the local zenith ($\cos \theta_z = 1$). From Eq. (11), this yields

$$\mathcal{E}_{\max} = \frac{A_0}{\omega_{\text{Earth}}} 2\pi . \quad (12)$$

Therefore, the normalized exposure becomes

$$\omega(\delta) = \frac{\mathcal{E}(\delta)}{\mathcal{E}_{\max}} = \frac{1}{\pi} (\alpha_m \sin \lambda \sin \delta + \cos \lambda \cos \delta \sin \alpha_m) , \quad (13)$$

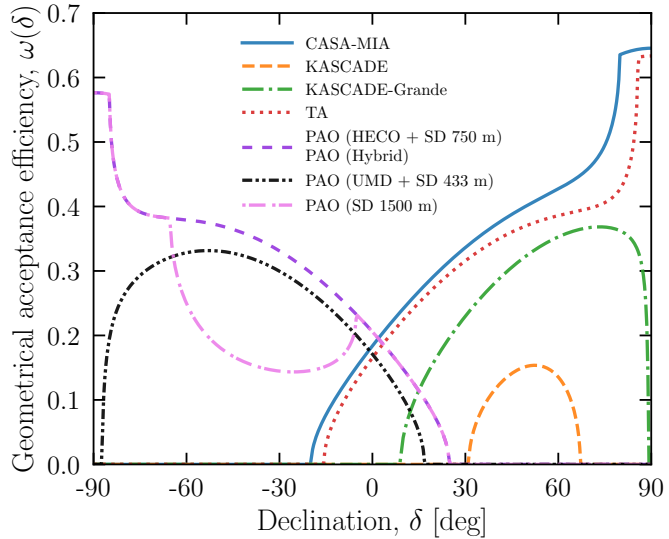


FIG. 2. Geometrical acceptance efficiency $\omega(\delta)$ as a function of the declination δ , for different UHE gamma-ray detectors shown with distinct curve styles. The configurations HECO + SD 750 m and Hybrid of the PAO detector share the same geometrical acceptance efficiency as their zenith angle ranges are equal (see Tab. I).

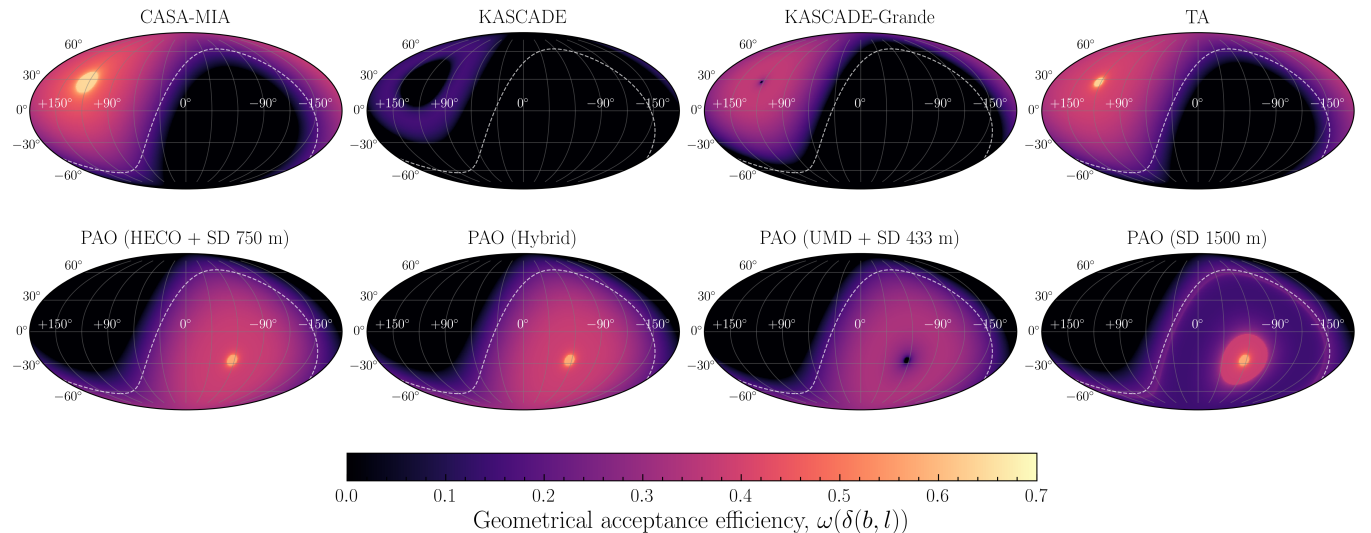


FIG. 3. FOV in galactic coordinates for each experiment considered in this study, with color grading indicating the geometrical acceptance efficiency $\omega(\delta(b, l))$ defined in Eq. (13).

where α_m is given by Eq. (8). Compared to the expression given in Ref. [70], Eq. (13) is by construction $0 \leq \omega(\delta) \leq 1$. Its value reflects both how long a source stays within the FOV and how favorably it transits in altitude. Sources that pass closer to the local zenith contribute more significantly than those remaining near the visibility limit, even for comparable visibility times. This refinement provides an essential geometrical weighting factor for the calculation of fluxes in realistic models of experiments monitoring large portions of the sky.

In Figs. 2 and 3 we show the resulting acceptance profiles for all experiments considered in this work. Specifically, Fig. 2 illustrates the geometrical acceptance efficiency as a function of the declination δ . The shape and width of each curve are determined by the detector latitude λ and zenith cut θ_m , which define the declination interval contributing to the exposure (see Eq. (10)). On the other hand, Fig. 3 displays the quantity $\omega(\delta)$ as a function of the galactic coordinates b and l , thus clearly indicating the FOV of each experiment as the colored regions.

III. GAMMA-RAY FLUX FROM HEAVY DECAYING DARK MATTER

A possible origin of UHE gamma rays is the decay of very massive DM particles. The overall gamma-ray signal expected from DM includes several components, arising from both prompt and secondary radiation produced in the Galaxy and beyond. In this study, we restrict ourselves to the prompt galactic emission, which dominates the spectrum at the highest photon energies reachable in DM-decay scenarios, while omitting the extragalactic contribution because it is heavily attenuated at UHE energies through $\gamma\gamma$ interactions. Furthermore, we also disregard the secondary galactic emission from Inverse Compton scattering of electrons and positrons on low-energy photon backgrounds (see, e.g., Ref. [31]). Indeed, this component is typically subleading compared with the prompt galactic one, and we have verified that its inclusion would not significantly impact our conclusions. As will be demonstrated later, this simplified approach is adequate for deriving strong and comprehensive gamma-ray constraints on dark matter, using observations that span several decades in energy, ranging from 10^5 up to 10^{11} GeV (see Tab. I).

The UHE gamma-ray flux from the prompt galactic emission of DM decays is expressed by

$$\frac{d\Phi_\gamma}{dE_\gamma d\Omega}(E_\gamma, b, l) = \frac{1}{4\pi m_{\text{DM}} \tau_{\text{DM}}} \frac{dN_\gamma}{dE_\gamma} \int_0^\infty \rho_{\text{DM}}(r(s, b, l)) e^{-\tau_{\gamma\gamma}(E_\gamma, s, b, l)} ds. \quad (14)$$

Here, m_{DM} and τ_{DM} respectively represent the mass and lifetime of the DM particle and purely depend on the nature of the DM candidate. The term $dN_\gamma/dE_\gamma(E_\gamma)$ is the energy spectrum of the generated photons and depends on the specific DM decay channel, which we compute using the `HDMSpectra` code [74] assuming a 100% branching ratio at a time. The integral term is related to astrophysical quantities through the galactic DM density distribution ρ_{DM} and the transmission factor (with $\tau_{\gamma\gamma}$ being the optical depth) due to high-energy photon interactions with the photon fields in the galaxy. These quantities depend on the line-of-sight s , the galactic angular coordinates (b, l) , and the galactocentric radial distance r defined as

$$r(s, b, l) = \sqrt{s^2 + R_\odot^2 - 2sR_\odot \cos b \cos l}, \quad (15)$$

where we fix the Sun's galactocentric distance to be $R_\odot = 8.178$ kpc according to the analyses in Refs. [69, 75].

To enable a direct comparison with existing bounds on the diffuse UHE gamma-ray flux, from Eq. (14) we evaluate the angle-averaged integral photon flux, which for each experiment is defined as

$$\Phi_\gamma(E_\gamma) = \frac{1}{\Delta\Omega_{\text{exp}}} \int_{E_\gamma}^\infty dE'_\gamma \int_{\Delta\Omega_{\text{exp}}} \frac{d\Phi_\gamma}{dE'_\gamma d\Omega} d\Omega = \frac{1}{4\pi m_{\text{DM}} \tau_{\text{DM}}} \int_{E_\gamma}^\infty \mathcal{D}_{\text{exp}}(E'_\gamma) \frac{dN_\gamma}{dE'_\gamma} \Big|_{E'_\gamma} ds, \quad (16)$$

where $\Delta\Omega_{\text{exp}}$ is the FOV of the experiment, and $\mathcal{D}_{\text{exp}}(E_\gamma)$ is the energy-dependent \mathcal{D} -factor defined as

$$\mathcal{D}_{\text{exp}}(E_\gamma) = \frac{1}{\Delta\Omega_{\text{exp}}} \int_{\Delta\Omega_{\text{exp}}} d\Omega \int_0^\infty \rho_{\text{DM}}(r(s, b, l)) e^{-\tau_{\gamma\gamma}(E_\gamma, s, b, l)} \omega_{\text{exp}}(\delta(b, l)) ds, \quad (17)$$

with $\omega_{\text{exp}}(\delta)$ being the geometrical acceptance efficiency of the experiment given in Eq. (13). As will be discussed later, taking into account the quantity $\omega_{\text{exp}}(\delta)$ in the definition of the \mathcal{D} -factor is crucial for obtaining reliable bounds on the DM lifetime from UHE gamma-ray surveys.

In the next two subsections, we detail the calculation of the optical depth and of the \mathcal{D} -factor, respectively. For the latter, we consider different experiments as well as different DM galactic distributions.

A. Gamma-ray attenuation in the Milky Way

The transmission factor in Eq. (14) involves the photon optical depth $\tau_{\gamma\gamma}$ which quantifies the attenuation due to $\gamma\gamma$ pair-production. This quantity can be written as the sum of two distinct components:

$$\tau_{\gamma\gamma}(E_\gamma, s, b, l) = \tau_{\gamma\gamma}^{\text{CMB}}(E_\gamma, s) + \tau_{\gamma\gamma}^{\text{SL+IR}}(E_\gamma, s, b, l). \quad (18)$$

The first component represents pair creation due to interactions with photons of the Cosmic Microwave Background (CMB). Owing to the isotropic and spatially uniform nature of the CMB, its contribution to the optical depth takes the analytic form

$$\tau_{\gamma\gamma}^{\text{CMB}}(E_\gamma, s) = \frac{4T_{\text{CMB}} s}{\pi^2 E_\gamma^2} \int_{m_e}^\infty \varepsilon_c^3 \sigma_{\gamma\gamma}(\varepsilon_c) \ln \left(1 - e^{-\varepsilon_c^2/(E_\gamma T_{\text{CMB}})} \right) d\varepsilon_c, \quad (19)$$

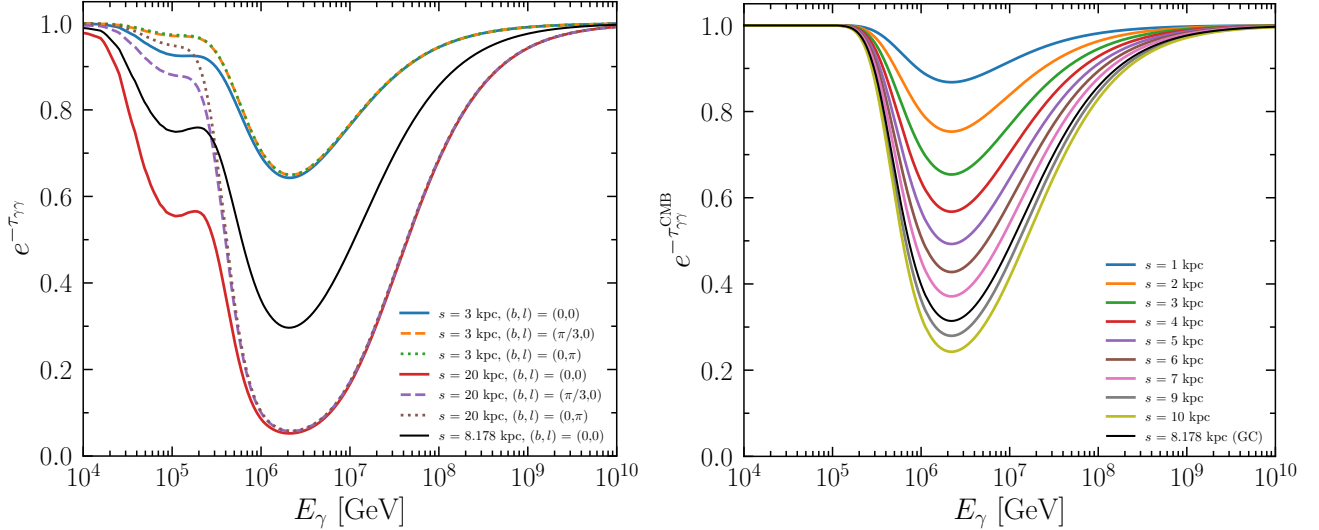


FIG. 4. Left panel: transmission factor for photons traversing both the CMB and the galactic SL+IR photon field computed for different distances of sources s , longitudes and latitudes (b, l) . Right panel: transmission factor for photons of energy E_γ considering only the CMB field.

where $\varepsilon_c = \sqrt{\varepsilon E_\gamma (1 - \cos \theta) / 2}$ denotes the photon center-of-momentum energy, $T_{\text{CMB}} = 2.348 \times 10^{-4}$ eV is the temperature of the CMB, and $\sigma_{\gamma\gamma}$ is the standard pair-production cross section,

$$\sigma_{\gamma\gamma} = \frac{\pi}{2} \frac{\alpha^2}{m_e^2} (1 - \beta^2) \left[(3 - \beta^4) \ln \left(\frac{1 + \beta}{1 - \beta} \right) - 2\beta(2 - \beta^2) \right]. \quad (20)$$

Here, α indicates the fine-structure constant, m_e is the electron mass, and $\beta = \sqrt{1 - 1/\mathfrak{s}}$ with $\mathfrak{s} = \varepsilon E_\gamma (1 - \cos \theta) / (2m_e^2) = \varepsilon_c^2 / m_e^2$. The second term, $\tau_{\gamma\gamma}^{\text{SL+IR}}$, describes absorption through pair production on galactic starlight and infrared radiation (SL+IR). In contrast to the CMB, this photon population varies significantly throughout the Milky Way. Under the assumption that the local radiation field is isotropic (though not spatially uniform), one may express its contribution as

$$\tau_{\gamma\gamma}^{\text{SL+IR}}(E_\gamma, s, b, l) = \int_0^s ds' \iint \sigma_{\gamma\gamma}(E_\gamma, \varepsilon) n_{\text{SL+IR}}[\varepsilon, \mathbf{x}(s', b, l)] \frac{1 - \cos \theta}{2} \sin \theta d\theta d\varepsilon, \quad (21)$$

with $n_{\text{SL+IR}}$ being the density of SL+IR photons obtained from the GALPROP framework [76]. Attenuation due to pair production from high energy photons interactions with the CMB significantly impacts the survival probability of high energy photons in the range between 10^6 GeV and 10^7 GeV, reaching an absorption peak at $\simeq 2 \times 10^6$ GeV, whereas the higher energies of the SL+IR photon field lower the energy threshold for the pair production mechanism resulting in an absorption peak at $\simeq 10^5$ GeV [77]. Unlike the uniform CMB background, the SL+IR photon density $n_{\text{SL+IR}}$ is modeled over the distributions of dust and stellar sources in the galaxy, resulting in a higher density of target photons in the galactic center and disk regions that rapidly decreases with latitude. This introduces a non trivial dependency of the optical depth over the position of the source relative to the observer. Models for the SL+IR photon energy density continue to be proposed based on updated near-, far-infrared and sub-millimeter emission data [78–80].

In Fig. 4, we show the transmission factor as a function of the photon energy focusing on the overall energy range observable by the considered experiments (summarized in Tab. I). We consider the total transmission coefficient from both SL+IR and CMB (left panel) and CMB only (right panel). The total transmission factor exhibits an absorption peak due to the SL+IR contribution at $\simeq 10^5$ GeV and becomes significant only in the vicinity of the galactic center ($b = 0, l = 0$) as it rapidly decreases with latitude. For experiments such as PAO and TA that observe the galactic center but are only sensible to the higher end of the UHE gamma-ray spectrum ($E_\gamma \gtrsim 10^7$ GeV), the SL+IR contribution is subdominant with respect to the CMB contribution. Likewise, absorption due to SL+IR radiation is also heavily suppressed for the experiments CASA-MIA and KASCADE which may still be marginally affected by the high-energy tail of the SL+IR component in the transmission factor. This suppression arises because the galactic center region does not fall within the FOV of these experiments, as shown in the Mollweide projections in Fig. 3. Consequently, in our calculations we always consider $\tau_{\gamma\gamma}(E_\gamma, s, b, l) \simeq \tau_{\gamma\gamma}^{\text{CMB}}(E_\gamma, s)$, omitting the contribution given by the SL+IR component to the absorption.

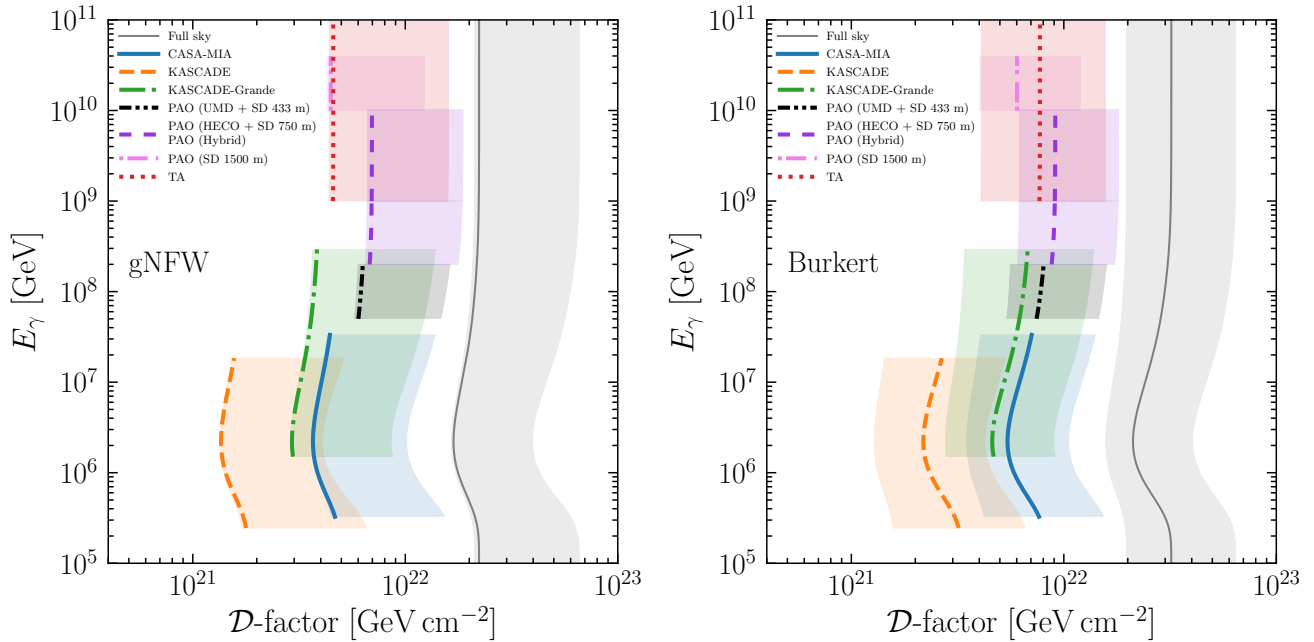


FIG. 5. \mathcal{D} -factor as a function of the gamma-ray energy computed for the full sky and for the experiments listed in Tab. I, shown with different colors. The x-axis and y-axis are swapped for better visualization. The left and right plots refer to the gNFW and Burkert DM profiles, respectively. The curves with distinct styles correspond to the fiducial DM profiles, while the shaded regions quantify the 2σ uncertainty on the DM-halo parameters from Ref. [69] (see text and Tab. II).

B. Dark matter distribution and \mathcal{D} -factor

DM density profiles are typically classified into cuspy and cored halo models, based on their behavior in the galaxy's inner regions. The cuspy models are expected to diverge as the galactocentric distance r approaches zero, while the cored models exhibit a finite central density in this limit.

In this work, we use the generalized Navarro–Frenk–White profile and the Burkert profile as representatives of these two classes, respectively. The gNFW profile takes the expression

$$\rho_{\text{gNFW}}(r) = \frac{\rho_s}{(r/R_s)^\gamma (1+r/R_s)^{3-\gamma}}, \quad (22)$$

where R_s is the scale radius, ρ_s is a normalization factor, and γ is the inner slope of the profile. The inner slope is typically considered to vary from 0.1 to 1.4. Setting $\gamma = 1$, we obtain the commonly-used NFW profile [81]. The Burkert profile is instead defined as [82]

$$\rho_{\text{Burk}}(r) = \frac{\rho_c R_c^3}{(r+R_c)(r^2+R_c^2)}, \quad (23)$$

where R_c is the core radius and ρ_c denotes the central density. In our study, we employ fiducial values for the parameters of the two profiles, specifically a local DM density $\rho_0 = 0.4 \text{ GeV/cm}^3$ and a characteristic radius $R_s = R_c = 25 \text{ kpc}$. We assign the slope of the gNFW profile a fiducial value of $\gamma = 1.0$, corresponding to the standard NFW profile. The normalization of the DM profiles is then determined from the local density through the relation $\rho_{\text{DM}}(R_\odot) = \rho_0$. These parameter selections enable effective comparisons with other studies, as these values are prevalent in the literature.

In Fig. 5 we display the \mathcal{D} -factor as a function of the gamma-ray energy for the gNFW and Burkert DM profiles in the left and right panels, respectively. The effect of the gamma-ray attenuation is visible for energies from $\sim 10^5$ to $\sim 10^7 \text{ GeV}$, where the \mathcal{D} -factor deviates from its constant value. Remarkably, we compare the \mathcal{D} -factor we find for the different experiments listed in Tab. I to the one computed over the full sky. The curves correspond to our fiducial choices for the parameters of the two profiles, while the shaded regions highlight the current uncertainty at 2σ CL on the \mathcal{D} -factor from the current measurements of the galactic DM distribution. Indeed, several sources of uncertainty must be taken into account when attempting to constrain the parameters of the DM density profiles

	Burkert profile	gNFW profile		
Full-sky \mathcal{D} -factor [10^{23} GeV cm $^{-2}$]	$\gamma = 0.1$	$\gamma = 1.0$	$\gamma = 1.4$	
Min value	2.48	2.67	2.76	2.86
Max value	8.10	8.29	5.71	4.46
Fiducial value	4.03	—	2.80	—

TABLE II. Minimum, maximum and fiducial values of the full-sky \mathcal{D} -factor at $E_\gamma = 10^9$ GeV for the Burkert and gNFW DM profiles according to the 2σ uncertainty from the determination of the galactic DM distribution [69]. The fiducial values correspond to a local DM density of $\rho_0 = 0.4$ GeV/cm 3 and a characteristic radius $R_s = R_c = 25$ kpc.

with the galactic rotation curves. Our position within the Milky Way leads to uncertainties in the determination of R_\odot and the Sun's circular velocity. Additional uncertainties arise from the limited knowledge of the baryonic mass components (bulge, stellar disk, and gas) [83], the corresponding normalization factors given by the microlensing optical depth for the bulge [84] and the local surface density for the stellar disk [85], and the systematic errors in the observational determination of the Milky Way rotation curves [86–88]. Hence, in order to take into account the astrophysical uncertainties, we determine the parameters defining the profiles in Eqs. (22) and (23) according to the 2σ contours provided in Ref. [69]. Specifically, we use the contours in which the Sun's galactocentric distance is fixed to the value $R_\odot = 8.178$, while the remaining parameters are profiled over following a frequentist method (for details, see Refs. [68, 89]).

We find that taking into account the FOV and the geometrical acceptance efficiency of each experiment reduces the \mathcal{D} -factor up to an order of magnitude (see the dashed orange curve for the KASCADE experiment). As will be discussed later, this result has a strong impact on the constraints on the DM parameter space. On the other hand, the uncertainty in the DM profile leads only to variations of a few in the \mathcal{D} -factor. This is also evident in Tab. II where we report the minimum, maximum and fiducial values of the full-sky \mathcal{D} -factor obtained by varying the DM-halo parameters within their 2σ uncertainties and fixing the gamma-ray energy at $E_\gamma = 10^9$ GeV (no attenuation). We emphasize that for the gNFW profile the minimum and the maximum values are both attained at a slope value of $\gamma = 0.1$, for which large values for the scale radius R_s are allowed. Moreover, the fiducial NFW profile yields a \mathcal{D} -factor that is nearly identical to the minimum gNFW value, thus explaining the curves in the left panel of Fig. 5.

IV. CONSTRAINTS ON THE DARK MATTER LIFETIME

We derive the limits on the parameter space of heavy decaying DM particles by comparing the predicted integral γ -ray flux with the observational upper bounds. Following the same procedure adopted in Ref. [36], for each dataset reported in Tab. I, we consider the test statistic (TS):

$$\text{TS}(m_{\text{DM}}, \tau_{\text{DM}}) = \sum_{i=1}^N \left(\frac{\Phi_\gamma(E_{\gamma,i}|m_{\text{DM}}, \tau_{\text{DM}}) - \Phi_{\gamma,i}^{\text{data}}}{\sigma_i} \right)^2, \quad (24)$$

where $\Phi_\gamma(E_{\gamma,i}|m_{\text{DM}}, \tau_{\text{DM}})$ is the DM-induced integral flux of Eq. (16), while $\Phi_{\gamma,i}^{\text{data}}$ and σ_i represent, respectively, the reported flux values and their uncertainties. Each term in the sum corresponds to one experimental energy bin. Because the measurements are published as upper limits, we simply take $\Phi_{\gamma,i}^{\text{data}} = 0$, and the quantities σ_i are reconstructed at the 68% CL according to the confidence level associated with each experimental constraint.

We set the 95% CL lower bound on the lifetime for DM masses from 10^7 to 10^{15} GeV by assuming that any potential signal originates solely from DM decay. The requirement that the hypothesis of zero observed photon events is excluded with more than 95% probability translates into the condition $\text{TS} = 2.76$. This threshold does not come from the standard χ^2 distribution because the flux measurements are restricted to be non-negative. Accounting for this constraint leads to the modified probability density

$$P(x) = \frac{e^{-x/2}}{\sqrt{2\pi x}} \frac{1 + \Theta(\lambda - x)}{1 + \text{Erf}(\lambda/\sqrt{2})}, \quad (25)$$

with $x = \text{TS}$ and $\lambda = \sum_{i=1}^N [\Phi_\gamma(E_{\gamma,i}|m_{\text{DM}}, \tau_{\text{DM}})/\sigma_i]^2$, which corresponds to the TS evaluated at $\Phi_{\gamma,i}^{\text{data}} = 0$. The Heaviside function Θ appears because of the positivity constraint on the measured fluxes. In the limit of large λ ,

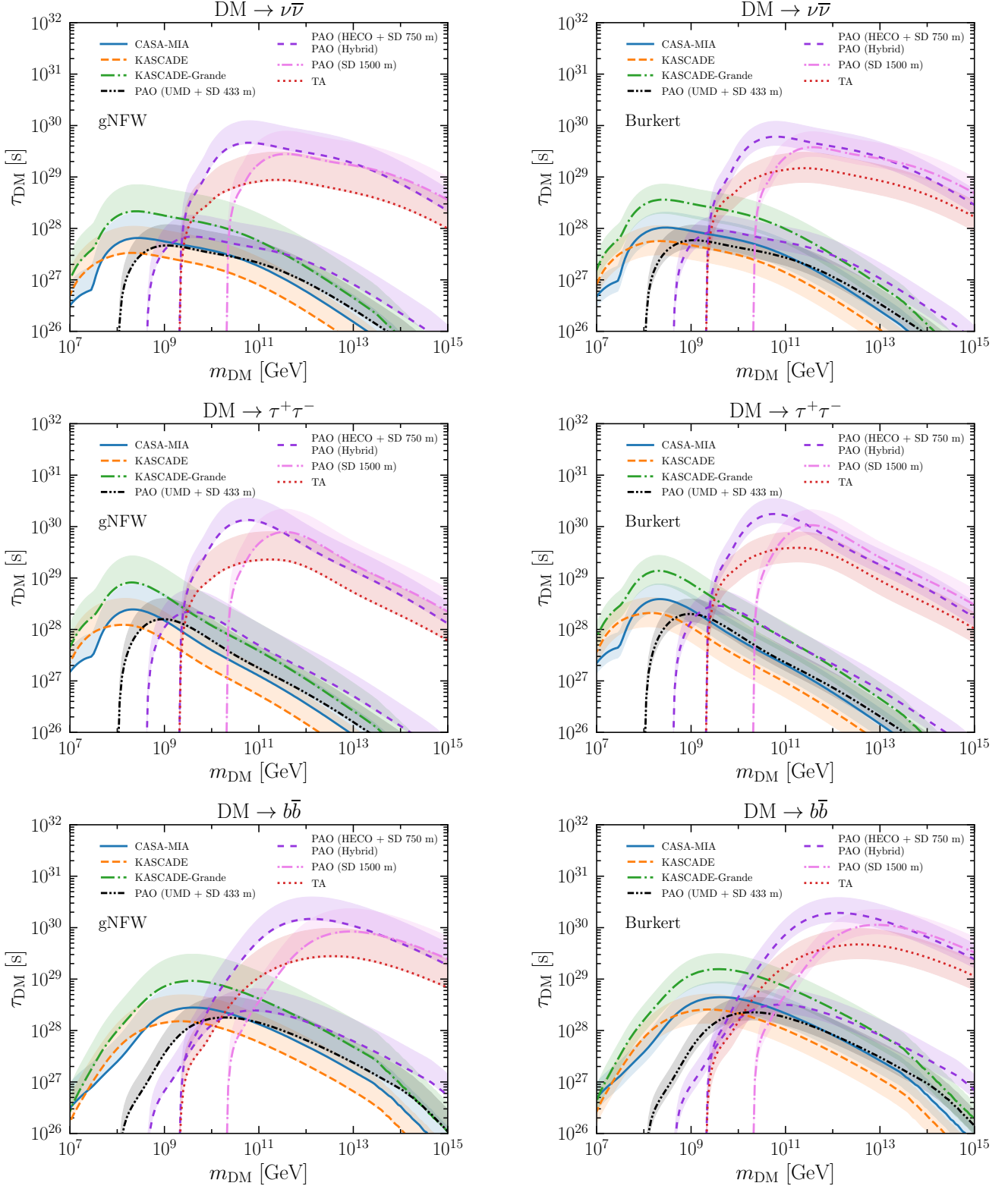


FIG. 6. Lower bounds on the lifetime of decaying DM particles at 95% CL for the channels $DM \rightarrow \nu\bar{\nu}$ (upper plots), $DM \rightarrow \tau^+\tau^-$ (middle plots) and $DM \rightarrow b\bar{b}$ (lower plots) assuming the gNFW (left plots) and Burkert (right plots) profiles. Different styles correspond to the datasets reported in Tab. I. The lines show the constraints assuming the fiducial values for the DM profiles, while the bands cover the 2σ uncertainty on the \mathcal{D} -factor (see Fig. 5).

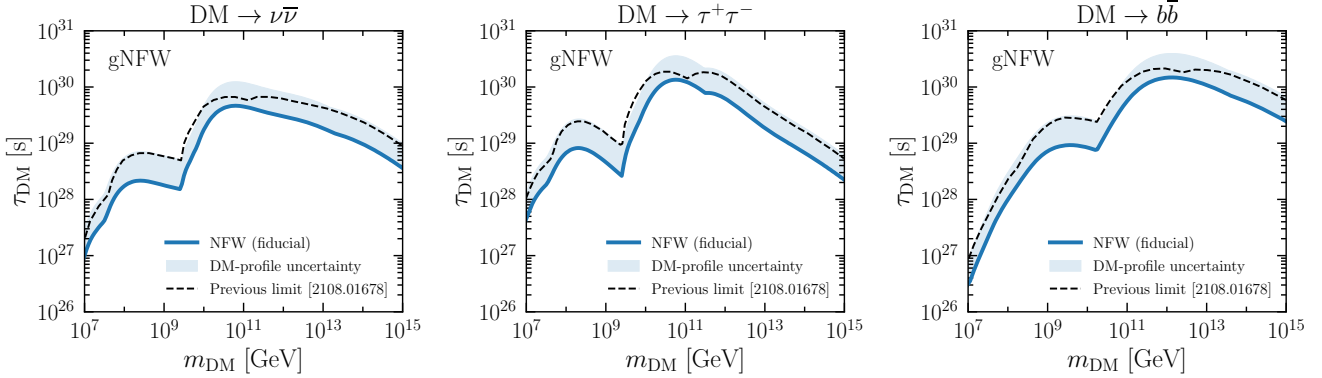


FIG. 7. Comparison between the overall UHE gamma-ray bounds obtained in the present work (blue solid lines) and the ones obtained in Ref. [36] (black dashed lines), considering different DM decay channels and assuming the fiducial NFW profile (i.e. gNFW with slope $\gamma = 1$, see Eq. (22)) with $\rho_0 = 0.4 \text{ GeV/cm}^3$ and $R_s = 25.0 \text{ kpc}$. The shaded regions correspond to the 2σ uncertainty according to the current determination of the parameters of the gNFW profile.

when the predicted fluxes are well above zero, the expression converges to the usual χ^2 behavior. Since in our case the measured TS is equal to λ , the 95% exclusion value is obtained by imposing $\lambda = 2.76$.

In Fig. 6, we show the 95% confidence-level lower limits on the lifetime of decaying DM particles for three representative decay channels, organized into upper, middle, and lower panels corresponding to $\text{DM} \rightarrow \nu\bar{\nu}$, $\text{DM} \rightarrow \tau^+\tau^-$, and $\text{DM} \rightarrow b\bar{b}$, respectively (see Appendix A for other decay channels). Each channel is evaluated under two benchmark assumptions for the galactic DM distribution: a cuspy gNFW profile (left column) and a cored Burkert profile (right column). The various line styles reflect the different observational datasets summarized in Tab. I, enabling a clear comparison of their relative constraining power over the full DM mass range. The different curves represent the limits obtained using the fiducial values of the respective halo profiles, while the surrounding shaded bands illustrate the astrophysical uncertainties by spanning the 2σ range of the corresponding \mathcal{D} -factor, as derived in the previous Section. This figure highlights both the dependence of the inferred limits on the assumed galactic density profile and the degree to which halo-model uncertainties propagate into the final constraints. In Fig. 7, we show a direct comparison between the overall UHE gamma-ray constraints derived in the present work and the corresponding limits reported in Ref. [36]. The blue solid lines represent our updated results, while the black dashed lines indicate the previous bounds. The figure considers the three representative decay channels, all evaluated assuming the fiducial NFW profile. As for the previous figure, the shaded regions surrounding the curves denote the 2σ uncertainty on the limits, which arises from the current determination of the parameters of the gNFW profile. This comparison clearly illustrates the improvements achieved with the present analysis. Specifically, we find that, despite considering a higher DM halo density and the updated limits on the UHE gamma-ray diffuse flux (e.g. from TA and PAO), the resulting bounds are weaker due to the inclusion of the geometrical acceptance efficiency of each experiment. The figure also shows how the derived limits depend on the choice of halo-profile parameters, indicating that uncertainties in the DM distribution affect the robustness of the constraints.

In Fig. 8, we show the maximum all-sky single-flavor neutrino and antineutrino flux that is allowed by the gamma-ray limits on the SHDM particle decays. The neutrino flux is computed by summing the galactic and extragalactic components and averaging over the full sky. The shaded regions indicate the envelope resulting from the superposition of the neutrino fluxes corresponding to SHDM masses in the range 10^6 - 10^{15} GeV. For each SHDM mass, we consider the lowest allowed values for the SHDM lifetime according to the bounds derived in the present work and to the ones from LHAASO Collaboration [38] after a proper rescaling of the DM halo density to the current estimate. These regions therefore illustrate the theoretical uncertainty associated with the SHDM parameter space and the decay-mode channels. For comparison, we also include existing experimental measurements and limits: the IceCube neutrino flux measurements (the Northern Sky Tracks (NST), the High-Energy Starting Events (HESE), and the Glashow resonance event) at energies below 10^8 GeV [90-92], the flux estimate inferred from the KM3-230213A event [52], and the upper bounds (shown as dashed lines) obtained by ANTARES [93], IceCube in the Extremely High-Energy (EHE) regime [94], and the Pierre Auger Observatory [95]. The comparison highlights the interplay between gamma-ray and neutrino observations in probing the SHDM decay scenarios. Specifically, hadronic decay channels (e.g. $\text{DM} \rightarrow b\bar{b}$) result to be more constrained by the gamma-ray data while being consistent with current neutrino data. On the other hand, the leptonic channels (e.g. $\text{DM} \rightarrow \tau^+\tau^-$ and $\text{DM} \rightarrow \nu\bar{\nu}$) are better probed by neutrino measurements especially for SHDM masses below 10^8 GeV. Interestingly, we find that the leptonic channels are compatible with the flux expected from the KM3-230213A event (a dedicated analysis is beyond the scope of the

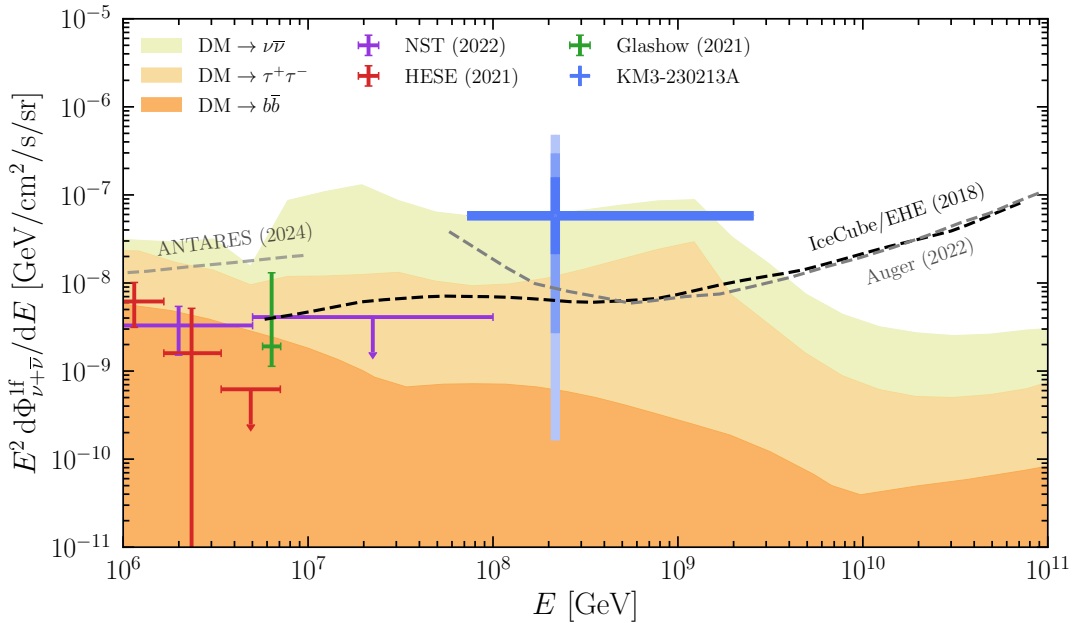


FIG. 8. Maximum all-sky single-flavor neutrino and antineutrino flux from the decays of SHDM particles as constrained by gamma-ray data. The shaded regions represent the overlap of the neutrino fluxes related to different SHDM masses ranging from 10^6 to 10^{15} GeV for different decay channels. Also shown are the IceCube data below 10^8 GeV [90–92], the flux estimate from the KM3-230213A event [52], and the upper bounds (dashed lines) placed by ANTARES [93], IceCube/EHE [94] and Pierre Auger [95] (from left to right).

present work).

V. CONCLUSIONS

The indirect approach based on the observation of high-energy gamma rays produced by the decay of dark matter particles constitutes an important strategy for placing stringent constraints on the dark matter parameters. In this regard, we have re-examined the constraints on super-heavy dark matter lifetimes, in the mass range from 10^7 to 10^{15} GeV, using the ultra-high-energy gamma-ray searches carried out by the CASA-MIA, KASCADE, KASCADE-Grande, Pierre Auger Observatory and Telescope Array experiments, placing emphasis on realistic instrument response and astrophysical uncertainties. In particular, by folding the field-of-view and the geometrical acceptance of each experiment into the analysis, we obtain dark matter lifetime limits that are slightly more conservative than those in previous works but substantially more faithful to the true sensitivity of current air-shower arrays. Indeed, accounting for the directional dependency is crucial when analyzing the anisotropic gamma-ray fluxes expected from dark matter decays, which are influenced by the spatial distribution of the galactic halo. Across a variety of two-body decay channels and halo models (NFW and Burkert profiles), the present ultra-high-energy gamma-ray data exclude sizeable regions of the parameter space of super-heavy dark matter particles and complement limits from neutrinos. Importantly, our results elucidate the potential tension between the upper bounds on the gamma-ray emission and the possible interpretation of the KM3-230213A event in the context of decaying super-heavy dark matter models.

ACKNOWLEDGEMENTS

We acknowledge the support by the following research projects funded by the Istituto Nazionale di Fisica Nucleare (INFN): MC and NS by the TAsP (Theoretical Astroparticle Physics) project; SC and FS by the QGSKY (Quantum Gravity in the SKY) project; by the TEONGRAV project; and VN by the MoonLIGHT-2 project. The work of NS is further supported by the research grant number 2022E2J4RK “PANTHEON: Perspectives in Astroparticle and Neutrino THEory with Old and New messengers” under the program PRIN 2022 funded by the Italian Ministero dell’Università e della Ricerca (MUR).

This work has been carried out in the context of the course “Introduction to Astroparticle Physics”, taught by MC and NS, and offered by the PhD program “Cosmology, Space Science & Space Technology (SPACE)” at the Scuola Superiore Meridionale (SSM). The numerical analysis was performed by the PhD students SC, VMG, VN, FS, and AT, who were organized into independent groups, each dedicated to a specific section. The entire project was coordinated under the supervision of MC and NS, who collected and checked all the numerical codes developed by the students. All the authors participated in writing the manuscript and preparing the figures.

[1] G. Bertone, D. Hooper, and J. Silk, Particle dark matter: Evidence, candidates and constraints, *Phys. Rept.* **405**, 279 (2005), [arXiv:hep-ph/0404175](https://arxiv.org/abs/hep-ph/0404175).

[2] G. Bertone and D. Hooper, History of dark matter, *Rev. Mod. Phys.* **90**, 045002 (2018), [arXiv:1605.04909](https://arxiv.org/abs/1605.04909) [astro-ph.CO].

[3] F. Kahlhoefer, Review of LHC Dark Matter Searches, *Int. J. Mod. Phys. A* **32**, 1730006 (2017), [arXiv:1702.02430](https://arxiv.org/abs/1702.02430) [hep-ph].

[4] J. Billard *et al.*, Direct detection of dark matter—APPEC committee report*, *Rept. Prog. Phys.* **85**, 056201 (2022), [arXiv:2104.07634](https://arxiv.org/abs/2104.07634) [hep-ex].

[5] R. Alves Batista *et al.*, EuCAPT White Paper: Opportunities and Challenges for Theoretical Astroparticle Physics in the Next Decade, (2021), [arXiv:2110.10074](https://arxiv.org/abs/2110.10074) [astro-ph.HE].

[6] B. R. Greene, T. Prokopec, and T. G. Roos, Inflaton decay and heavy particle production with negative coupling, *Phys. Rev. D* **56**, 6484 (1997), [arXiv:hep-ph/9705357](https://arxiv.org/abs/hep-ph/9705357).

[7] D. J. H. Chung, E. W. Kolb, and A. Riotto, Superheavy dark matter, *Phys. Rev. D* **59**, 023501 (1998), [arXiv:hep-ph/9802238](https://arxiv.org/abs/hep-ph/9802238).

[8] K. Benakli, J. R. Ellis, and D. V. Nanopoulos, Natural candidates for superheavy dark matter in string and M theory, *Phys. Rev. D* **59**, 047301 (1999), [arXiv:hep-ph/9803333](https://arxiv.org/abs/hep-ph/9803333).

[9] E. W. Kolb, D. J. H. Chung, and A. Riotto, WIMPzillas!, *AIP Conf. Proc.* **484**, 91 (1999), [arXiv:hep-ph/9810361](https://arxiv.org/abs/hep-ph/9810361).

[10] M. Chianese and A. Merle, A Consistent Theory of Decaying Dark Matter Connecting IceCube to the Sesame Street, *JCAP* **04**, 017, [arXiv:1607.05283](https://arxiv.org/abs/1607.05283) [hep-ph].

[11] K. Kannike, A. Racioppi, and M. Raidal, Super-heavy dark matter – Towards predictive scenarios from inflation, *Nucl. Phys. B* **918**, 162 (2017), [arXiv:1605.09378](https://arxiv.org/abs/1605.09378) [hep-ph].

[12] E. W. Kolb and A. J. Long, Superheavy dark matter through Higgs portal operators, *Phys. Rev. D* **96**, 103540 (2017), [arXiv:1708.04293](https://arxiv.org/abs/1708.04293) [astro-ph.CO].

[13] H. Kim and E. Kuflik, Superheavy Thermal Dark Matter, *Phys. Rev. Lett.* **123**, 191801 (2019), [arXiv:1906.00981](https://arxiv.org/abs/1906.00981) [hep-ph].

[14] E. Dudas, L. Heurtier, Y. Mambrini, K. A. Olive, and M. Pierre, Model of metastable EeV dark matter, *Phys. Rev. D* **101**, 115029 (2020), [arXiv:2003.02846](https://arxiv.org/abs/2003.02846) [hep-ph].

[15] T. Hambye, M. Lucca, and L. Vanderheyden, Dark matter as a heavy thermal hot relic, *Phys. Lett. B* **807**, 135553 (2020), [arXiv:2003.04936](https://arxiv.org/abs/2003.04936) [hep-ph].

[16] S. Ling and A. J. Long, Superheavy scalar dark matter from gravitational particle production in α -attractor models of inflation, *Phys. Rev. D* **103**, 103532 (2021), [arXiv:2101.11621](https://arxiv.org/abs/2101.11621) [astro-ph.CO].

[17] R. Allahverdi, C. Arina, M. Chianese, M. Cicoli, F. Maltoni, D. Massaro, and J. K. Osiński, Phenomenology of superheavy decaying dark matter from string theory, *JHEP* **02**, 192, [arXiv:2312.00136](https://arxiv.org/abs/2312.00136) [hep-ph].

[18] K. Murase and J. F. Beacom, Constraining Very Heavy Dark Matter Using Diffuse Backgrounds of Neutrinos and Cascaded Gamma Rays, *JCAP* **10**, 043, [arXiv:1206.2595](https://arxiv.org/abs/1206.2595) [hep-ph].

[19] A. Esmaili, A. Ibarra, and O. L. G. Peres, Probing the stability of superheavy dark matter particles with high-energy neutrinos, *JCAP* **11**, 034, [arXiv:1205.5281](https://arxiv.org/abs/1205.5281) [hep-ph].

[20] A. Esmaili and P. D. Serpico, Are IceCube neutrinos unveiling PeV-scale decaying dark matter?, *JCAP* **11**, 054, [arXiv:1308.1105](https://arxiv.org/abs/1308.1105) [hep-ph].

[21] C. Rott, K. Kohri, and S. C. Park, Superheavy dark matter and IceCube neutrino signals: Bounds on decaying dark matter, *Phys. Rev. D* **92**, 023529 (2015), [arXiv:1408.4575](https://arxiv.org/abs/1408.4575) [hep-ph].

[22] S. M. Boucenna, M. Chianese, G. Mangano, G. Miele, S. Morisi, O. Pisanti, and E. Vitagliano, Decaying Leptophilic Dark Matter at IceCube, *JCAP* **12**, 055, [arXiv:1507.01000](https://arxiv.org/abs/1507.01000) [hep-ph].

[23] A. Esmaili and P. D. Serpico, Gamma-ray bounds from EAS detectors and heavy decaying dark matter constraints, *JCAP* **10**, 014, [arXiv:1505.06486](https://arxiv.org/abs/1505.06486) [hep-ph].

[24] K. Murase, R. Laha, S. Ando, and M. Ahlers, Testing the Dark Matter Scenario for PeV Neutrinos Observed in IceCube, *Phys. Rev. Lett.* **115**, 071301 (2015), [arXiv:1503.04663](https://arxiv.org/abs/1503.04663) [hep-ph].

[25] T. Cohen, K. Murase, N. L. Rodd, B. R. Safdi, and Y. Soreq, γ -ray Constraints on Decaying Dark Matter and Implications for IceCube, *Phys. Rev. Lett.* **119**, 021102 (2017), [arXiv:1612.05638](https://arxiv.org/abs/1612.05638) [hep-ph].

[26] O. K. Kalashev and M. Y. Kuznetsov, Constraining heavy decaying dark matter with the high energy gamma-ray limits, *Phys. Rev. D* **94**, 063535 (2016), [arXiv:1606.07354](https://arxiv.org/abs/1606.07354) [astro-ph.HE].

[27] M. G. Aartsen *et al.* (IceCube), Search for neutrinos from decaying dark matter with IceCube, *Eur. Phys. J. C* **78**, 831 (2018), [arXiv:1804.03848](https://arxiv.org/abs/1804.03848) [astro-ph.HE].

[28] M. Kachelriess, O. E. Kalashev, and M. Y. Kuznetsov, Heavy decaying dark matter and IceCube high energy neutrinos, *Phys. Rev. D* **98**, 083016 (2018), [arXiv:1805.04500](https://arxiv.org/abs/1805.04500) [astro-ph.HE].

[29] M. Chianese, D. F. G. Fiorillo, G. Miele, S. Morisi, and O. Pisanti, Decaying dark matter at IceCube and its signature on

High Energy gamma experiments, *JCAP* **11**, 046, arXiv:1907.11222 [hep-ph].

[30] A. Dekker, M. Chianese, and S. Ando, Probing dark matter signals in neutrino telescopes through angular power spectrum, *JCAP* **09**, 007, arXiv:1910.12917 [hep-ph].

[31] K. Ishiwata, O. Macias, S. Ando, and M. Arimoto, Probing heavy dark matter decays with multi-messenger astrophysical data, *JCAP* **01**, 003, arXiv:1907.11671 [astro-ph.HE].

[32] M. Chianese, D. F. G. Fiorillo, R. Hajjar, G. Miele, S. Morisi, and N. Saviano, Heavy decaying dark matter at future neutrino radio telescopes, *JCAP* **05**, 074, arXiv:2103.03254 [hep-ph].

[33] A. Esmaili and P. D. Serpico, First implications of Tibet AS γ data for heavy dark matter, *Phys. Rev. D* **104**, L021301 (2021), arXiv:2105.01826 [hep-ph].

[34] T. N. Maity, A. K. Saha, A. Dubey, and R. Laha, Search for dark matter using sub-PeV γ -rays observed by Tibet AS γ , *Phys. Rev. D* **105**, L041301 (2022), arXiv:2105.05680 [hep-ph].

[35] C. Guépin, R. Aloisio, L. A. Anchordoqui, A. Cummings, J. F. Krizmanic, A. V. Olinto, M. H. Reno, and T. M. Venters, Indirect dark matter searches at ultrahigh energy neutrino detectors, *Phys. Rev. D* **104**, 083002 (2021), arXiv:2106.04446 [hep-ph].

[36] M. Chianese, D. F. G. Fiorillo, R. Hajjar, G. Miele, and N. Saviano, Constraints on heavy decaying dark matter with current gamma-ray measurements, *JCAP* **11**, 035, arXiv:2108.01678 [hep-ph].

[37] C. A. Argüelles, D. Delgado, A. Friedlander, A. Kheirandish, I. Safa, A. C. Vincent, and H. White, Dark matter decay to neutrinos, *Phys. Rev. D* **108**, 123021 (2023), arXiv:2210.01303 [hep-ph].

[38] Z. Cao *et al.* (LHAASO), Constraints on Heavy Decaying Dark Matter from 570 Days of LHAASO Observations, *Phys. Rev. Lett.* **129**, 261103 (2022), arXiv:2210.15989 [astro-ph.HE].

[39] B. Skrzypek, M. Chianese, C. A. Argüelles, and C. Delgado Argüelles, Multi-messenger high-energy signatures of decaying dark matter and the effect of background light, *JCAP* **01**, 037, arXiv:2205.03416 [astro-ph.HE].

[40] P. Abreu *et al.* (Pierre Auger), Limits to Gauge Coupling in the Dark Sector Set by the Nonobservation of Instanton-Induced Decay of Super-Heavy Dark Matter in the Pierre Auger Observatory Data, *Phys. Rev. Lett.* **130**, 061001 (2023), arXiv:2203.08854 [astro-ph.HE].

[41] P. Abreu *et al.* (Pierre Auger), Cosmological implications of photon-flux upper limits at ultrahigh energies in scenarios of Planckian-interacting massive particles for dark matter, *Phys. Rev. D* **107**, 042002 (2023), arXiv:2208.02353 [astro-ph.HE].

[42] S. Das, K. Murase, and T. Fujii, Revisiting ultrahigh-energy constraints on decaying superheavy dark matter, *Phys. Rev. D* **107**, 103013 (2023), arXiv:2302.02993 [astro-ph.HE].

[43] D. F. G. Fiorillo, V. B. Valera, M. Bustamante, and W. Winter, Searches for dark matter decay with ultrahigh-energy neutrinos endure backgrounds, *Phys. Rev. D* **108**, 103012 (2023), arXiv:2307.02538 [astro-ph.HE].

[44] D. M. H. Leung and K. C. Y. Ng, Improving HAWC dark matter constraints with inverse-Compton emission, *Phys. Rev. D* **110**, 103021 (2024), arXiv:2312.08989 [astro-ph.HE].

[45] A. Abdul Halim *et al.* (Pierre Auger), Constraints on metastable superheavy dark matter coupled to sterile neutrinos with the Pierre Auger Observatory, *Phys. Rev. D* **109**, L081101 (2024), arXiv:2311.14541 [hep-ph].

[46] P. Munbodh and S. Profumo, Astrophysical constraints from synchrotron emission on very massive decaying dark matter, *Phys. Rev. D* **110**, 043014 (2024), arXiv:2405.00798 [hep-ph].

[47] P. Sarmah, N. Das, D. Borah, S. Chakraborty, and P. Mehta, Constraining the superheavy dark matter origin of ultrahigh-energy cosmic rays with the Amaterasu event, *Phys. Rev. D* **111**, 083048 (2025), arXiv:2406.03174 [hep-ph].

[48] K. V. Berghaus, D. Hooper, and E. R. Simon, Searching for superheavy decaying particles with ultra-high-energy neutrino observatories, *JCAP* **07**, 067, arXiv:2502.12238 [hep-ph].

[49] C. Boehm, R. Laha, and T. N. Maity, LHAASO Galactic Plane γ -rays Strongly Constrain Heavy Dark Matter, (2025), arXiv:2509.07982 [hep-ph].

[50] A. Dubey and A. K. Saha, Breaking Dark: Hunting Heavy Decaying Dark Matter with Tibet AS γ and LHAASO-KM2A, (2025), arXiv:2509.08039 [hep-ph].

[51] M. Rocamora, P. De La Torre Luque, and M. A. Sánchez-Conde, Constraints on Ultra-heavy DM from TeV-PeV gamma-ray diffuse measurements, (2025), arXiv:2509.09609 [astro-ph.HE].

[52] S. Aiello *et al.* (KM3NeT), Observation of an ultra-high-energy cosmic neutrino with KM3NeT, *Nature* **638**, 376 (2025), [Erratum: Nature 640, E3 (2025)].

[53] B. Barman, A. Das, and P. Sarmah, What KM3-230213A event may tell us about the neutrino mass and dark matter, *Phys. Rev. D* **112**, 075014 (2025), arXiv:2504.01447 [hep-ph].

[54] Y. Jho, S. C. Park, and C. S. Shin, Superheavy supersymmetric dark matter as the origin of the KM3NeT ultrahigh energy signal, *Phys. Rev. D* **112**, 115004 (2025), arXiv:2503.18737 [hep-ph].

[55] R. Aloisio, A. Ambrosone, and C. Evoli, Constraining Super-Heavy Dark Matter with the KM3-230213A Neutrino Event, (2025), arXiv:2508.08779 [astro-ph.HE].

[56] K. Kohri, P. K. Paul, and N. Sahu, Super heavy dark matter origin of the PeV neutrino event: KM3-230213A, *Phys. Rev. D* **112**, L031703 (2025), arXiv:2503.04464 [hep-ph].

[57] D. Borah, N. Das, N. Okada, and P. Sarmah, Possible origin of the KM3-230213A neutrino event from dark matter decay, *Phys. Rev. D* **111**, 123022 (2025), arXiv:2503.00097 [hep-ph].

[58] S. Khan, J. Kim, and P. Ko, Linking the KM3-230213A neutrino event to dark matter decay and gravitational wave signals, *JCAP* **11**, 033, arXiv:2504.16040 [hep-ph].

[59] K. Murase, Y. Narita, and W. Yin, Superheavy dark matter from the natural inflation in light of the highest-energy astroparticle events, *JCAP* **10**, 109, arXiv:2504.15272 [hep-ph].

[60] M. C. Chantell *et al.* (CASA-MIA), Limits on the isotropic diffuse flux of ultrahigh-energy gamma radiation, *Phys. Rev.*

Lett. **79**, 1805 (1997), arXiv:astro-ph/9705246.

[61] T. Antoni *et al.* (KASCADE), KASCADE measurements of energy spectra for elemental groups of cosmic rays: Results and open problems, *Astropart. Phys.* **24**, 1 (2005), arXiv:astro-ph/0505413.

[62] W. D. Apel *et al.* (KASCADE Grande), KASCADE-Grande Limits on the Isotropic Diffuse Gamma-Ray Flux between 100 TeV and 1 EeV, *Astrophys. J.* **848**, 1 (2017), arXiv:1710.02889 [astro-ph.HE].

[63] R. U. Abbasi *et al.* (Telescope Array), Constraints on the diffuse photon flux with energies above 10^{18} eV using the surface detector of the Telescope Array experiment, *Astropart. Phys.* **110**, 8 (2019), arXiv:1811.03920 [astro-ph.HE].

[64] A. A. Halim *et al.* (Pierre Auger), Search for a diffuse flux of photons with energies above tens of PeV at the Pierre Auger Observatory, *JCAP* **05**, 061, arXiv:2502.02381 [astro-ph.HE].

[65] P. Abreu *et al.* (Pierre Auger), A Search for Photons with Energies Above 2×10^{17} eV Using Hybrid Data from the Low-Energy Extensions of the Pierre Auger Observatory, *Astrophys. J.* **933**, 125 (2022), arXiv:2205.14864 [astro-ph.HE].

[66] A. Abdul Halim *et al.* (Pierre Auger), Search for photons above 1018 eV by simultaneously measuring the atmospheric depth and the muon content of air showers at the Pierre Auger Observatory, *Phys. Rev. D* **110**, 062005 (2024), arXiv:2406.07439 [astro-ph.HE].

[67] P. Abreu *et al.* (Pierre Auger), Search for Photons above 10^{19} eV with the Surface Detector of the Pierre Auger Observatory, *JCAP* **05**, 021, arXiv:2209.05926 [astro-ph.HE].

[68] M. Benito, A. Cuoco, and F. Iocco, Handling the Uncertainties in the Galactic Dark Matter Distribution for Particle Dark Matter Searches, *JCAP* **03**, 033, arXiv:1901.02460 [astro-ph.GA].

[69] M. Benito, F. Iocco, and A. Cuoco, Uncertainties in the Galactic Dark Matter distribution: An update, *Phys. Dark Univ.* **32**, 100826 (2021), arXiv:2009.13523 [astro-ph.GA].

[70] P. Sommers, Cosmic ray anisotropy analysis with a full-sky observatory, *Astropart. Phys.* **14**, 271 (2001), arXiv:astro-ph/0004016.

[71] P. Abreu *et al.* (Pierre Auger), The Exposure of the Hybrid Detector of the Pierre Auger Observatory, *Astropart. Phys.* **34**, 368 (2011), arXiv:1010.6162 [astro-ph.HE].

[72] A. Esmaili and P. D. Serpico, Gamma-ray bounds from EAS detectors and heavy decaying dark matter constraints, *JCAP* **10**, 014, arXiv:1505.06486 [hep-ph].

[73] R. M. Green, *Spherical Astronomy* (Cambridge University Press, 1985).

[74] C. W. Bauer, N. L. Rodd, and B. R. Webber, Dark matter spectra from the electroweak to the Planck scale, *JHEP* **06**, 121, arXiv:2007.15001 [hep-ph].

[75] R. Abuter *et al.* (Gravity), A geometric distance measurement to the Galactic center black hole with 0.3% uncertainty, *Astron. Astrophys.* **625**, 10.1051/0004-6361/201935656 (2019), arXiv:1904.05721 [astro-ph.GA].

[76] *GALPROP* (2025).

[77] W. S. V. Moskalenko, A. Porter, Attenuation Of VHE Gamma rays by the milky way interstellar radiation field, *The Astrophysical Journal* **640**, 10.1086/503524 (April 2006).

[78] S. Vernetto and P. Lipari, Absorption of very high energy gamma rays in the Milky Way, *Phys. Rev. D* **94**, 063009 (2016), arXiv:1608.01587 [astro-ph.HE].

[79] T. A. Porter, G. Johannesson, and I. V. Moskalenko, High-Energy Gamma Rays from the Milky Way: Three-Dimensional Spatial Models for the Cosmic-Ray and Radiation Field Densities in the Interstellar Medium, *Astrophys. J.* **846**, 67 (2017), arXiv:1708.00816 [astro-ph.HE].

[80] C. C. Popescu, R. Yang, R. J. Tuffs, G. Natale, M. Rushton, and F. Aharonian, A radiation transfer model for the Milky-Way: I. Radiation fields and application to High Energy Astrophysics, *Mon. Not. Roy. Astron. Soc.* **470**, 2539 (2017), arXiv:1705.06652 [astro-ph.GA].

[81] J. F. Navarro, C. S. Frenk, and S. D. M. White, A Universal density profile from hierarchical clustering, *Astrophys. J.* **490**, 493 (1997), arXiv:astro-ph/9611107.

[82] A. Burkert, The Structure of dark matter halos in dwarf galaxies, *Astrophys. J. Lett.* **447**, L25 (1995), arXiv:astro-ph/9504041.

[83] M. Pato, F. Iocco, and G. Bertone, Dynamical constraints on the dark matter distribution in the Milky Way, *JCAP* **12**, 001, arXiv:1504.06324 [astro-ph.GA].

[84] P. Popowski *et al.* (MACHO), Microlensing optical depth towards the galactic bulge using clump giants from the MACHO survey, *Astrophys. J.* **631**, 879 (2005), arXiv:astro-ph/0410319.

[85] J. Bovy and H.-W. Rix, A Direct Dynamical Measurement of the Milky Way's Disk Surface Density Profile, Disk Scale Length, and Dark Matter Profile at 4 kpc $\lesssim R \lesssim$ 9 kpc, *Astrophys. J.* **779**, 115 (2013), arXiv:1309.0809 [astro-ph.GA].

[86] Y. Sofue, Pseudo Rotation Curve connecting the Galaxy, Dark Halo, and Local Group, *Publ. Astron. Soc. Jap.* **61**, 153 (2009), arXiv:0811.0860 [astro-ph].

[87] Y. Sofue, M. Honma, and T. Omodaka, Unified Rotation Curve of the Galaxy – Decomposition into de Vaucouleurs Bulge, Disk, Dark Halo, and the 9-kpc Rotation Dip –, *Publ. Astron. Soc. Jap.* **61**, 227 (2009), arXiv:0811.0859 [astro-ph].

[88] Y. Sofue, Rotation Curve and Mass Distribution in the Galactic Center — From Black Hole to Entire Galaxy —, *Publ. Astron. Soc. Jap.* **65**, 118 (2013), arXiv:1307.8241 [astro-ph.GA].

[89] W. A. Rolke, A. M. Lopez, and J. Conrad, Limits and confidence intervals in the presence of nuisance parameters, *Nucl. Instrum. Meth. A* **551**, 493 (2005), arXiv:physics/0403059.

[90] R. Abbasi *et al.*, Improved Characterization of the Astrophysical Muon–neutrino Flux with 9.5 Years of IceCube Data, *Astrophys. J.* **928**, 50 (2022), arXiv:2111.10299 [astro-ph.HE].

[91] R. Abbasi *et al.* (IceCube), The IceCube high-energy starting event sample: Description and flux characterization with 7.5

years of data, *Phys. Rev. D* **104**, 022002 (2021), arXiv:2011.03545 [astro-ph.HE].

[92] M. G. Aartsen *et al.* (IceCube), Detection of a particle shower at the Glashow resonance with IceCube, *Nature* **591**, 220 (2021), [Erratum: *Nature* 592, E11 (2021)], arXiv:2110.15051 [hep-ex].

[93] A. Albert *et al.* (ANTARES), Constraints on the energy spectrum of the diffuse cosmic neutrino flux from the ANTARES neutrino telescope, *JCAP* **08**, 038, arXiv:2407.00328 [astro-ph.HE].

[94] M. G. Aartsen *et al.* (IceCube), Differential limit on the extremely-high-energy cosmic neutrino flux in the presence of astrophysical background from nine years of IceCube data, *Phys. Rev. D* **98**, 062003 (2018), arXiv:1807.01820 [astro-ph.HE].

[95] A. Abdul Halim *et al.* (Pierre Auger), Latest results from the searches for ultra-high-energy photons and neutrinos at the Pierre Auger Observatory, *PoS ICRC2023*, 1488 (2023).

Appendix A: Lifetime bounds for several decay channels

We report in Fig. 9 the constraints obtained in the present work for several decay channels.

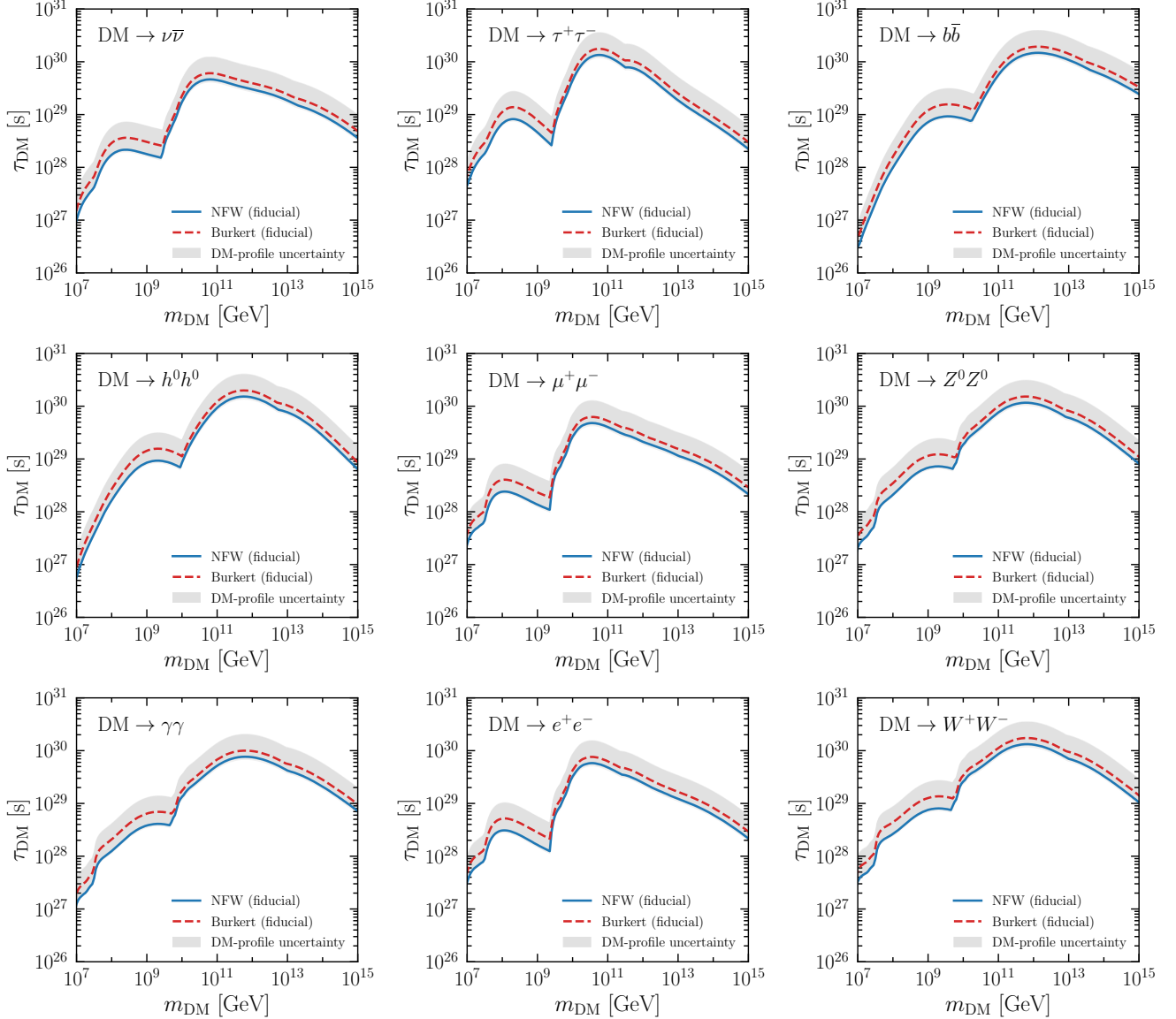


FIG. 9. Global lower bounds on the lifetime of decaying SHDM particles at 95% CL for various decay channels from UHE gamma-ray measurements. The solid blue (dashed red) lines correspond to the NFW (Burkert) density profile with the fiducial values $\rho_\odot = 0.4 \text{ GeV cm}^{-3}$ and $R_s = 25 \text{ kpc}$ ($R_c = 25 \text{ kpc}$). The shaded gray region represents the 2σ uncertainty on the DM lifetime limits from the determination of the galactic DM distribution.